KRONOS FUSION ENERGY

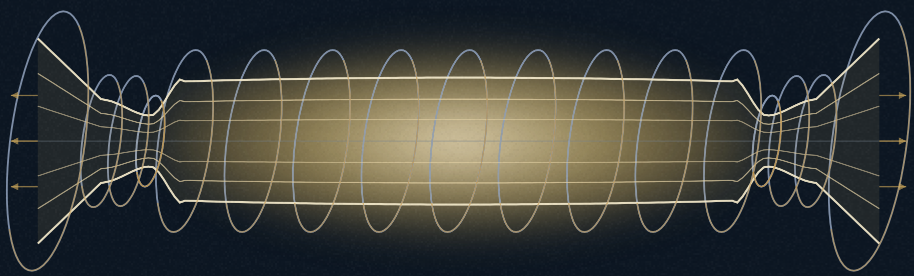

PAPER 2.54 · THE KRONOS 2026 SERIES

Velocity-Space Microstability at the DCLC Knee: Warm-Fill Requirements and Residual AIC Activity in a D–^{3}He Tandem-Mirror Burner

The end plug of a deuterium–helium-3 tandem-mirror burner confines the central-cell ions behind a large positive ambipolar potential, but the loss-cone velocity distribution that...

Read it live — 3-D model · physics validator · film series

BY P I FORD AND G L KULCINSKI

2026 · EDITORIAL EDITION

THE OFFICIAL RECORD

What this document is, and how to read its numbers

This is a combined editorial. It gathers, in one volume, the two design studies Kronos Fusion Energy released in 2026 — a compact spherical-tokamak tritium/helium-3 breeder and a deuterium–helium-3 tandem-mirror generator — together with the intellectual-property estate, the people, and, in the internal edition, the full commercial case. The scientific text is the same text that appears in the arXiv preprints and the journal submissions; the editorial adds the apparatus a reader needs to hold the whole program at once, and nothing in the physics is altered to fit it.

THE HONESTY STANCE IS THE ASSET

Every headline quantity carries an **evidence class** — DERIVED RECOMPUTED MEASURED REQUIREMENT — and, where a number is a modelled extrapolation rather than a demonstrated value, it is labelled as such and its downside is shown next to it. Several quantities in the underlying corpus moved after first publication; where a value has been withdrawn or restated, the record says so plainly. This is deliberate: a diligence team will find the load-bearing assumptions, so the document surfaces them first.

TWO EDITIONS

This volume is issued in two editions. The **public edition** (light) carries the physics and the design only — no dollar, price, or per-kilogram figure appears anywhere in it. The **internal edition** (dark) adds the economics, the funding architecture, and the defense-commercial analysis, and is marked *Confidential* accordingly; it is not for public distribution. Where the commercial case rests on a modelled assumption rather than a demonstrated one, it is labelled as such and its downside is shown alongside it, on the same terms as the physics.

TITLE	The Kronos Fleet — Hyperion · Aegis · MetroVolt: A Combined Design & Commercialization Study
AUTHOR	Priyanca Ford, Founder & CEO, on behalf of Kronos Fusion Energy
EDITION	2026 Combined Editorial · first issue
COMPANION WORKS	The five-paper arXiv drop — (1) Breeder, (2) Burner, (3) REBCO magnet & tape, (4) Direct Energy Conversion, (5) AI/ML/Quantum control — with matching numbered Zenodo deposits, plus the IOP journal and IAEA-FEC submissions. Patents were filed before the drop.
NAMING	Hyperion = the breeder; Aegis (defense) and MetroVolt (data-center) = one generator in two housings. Internal mode letters (D1, L) do not appear on public surfaces.
STATUS	Conceptual design & simulation study. Nothing herein is a construction commitment.

HOW TO READ THIS VOLUME

The fleet at a glance, and the way its numbers are marked

This volume opens with *Orientation*, presents the five research papers as a bound sequence, and closes with the *Apparatus*. *Foundations* sets out the three general results both machines rest on. *Paper One* is the Hyperion breeder; *Paper Two* the Aegis / MetroVolt generator; *Papers Three, Four and Five* are the enabling science — high-field REBCO magnets and tape, direct energy conversion, and the AI / ML / quantum control stack. A *Digital Twin & 3-D Model* part follows, then the *Environmental* profile. The *Economics* and levelized cost and the *Business Case* and diligence record appear in the internal edition only; the *Simulations* proof record and the Apparatus — patent portfolio, team, limitations, and sources — close both editions.

THE FLEET AT A GLANCE

	HYPERION	AEGIS	METROVOLT
Role	Strategic-isotope foundry	Defense installation power	Campus power
Machine	**Spherical tokamak**	**Tandem mirror**	**Tandem mirror**
Fuel	Deuterium–tritium	Deuterium–helium-3	Deuterium–helium-3
Delivers	Tritium · ^{3}He · 14 MeV n	Resilient installation power	Firm campus power
Physics bar	**Fusion gain only**	Closure (gates named)	Closure + lunar ^{3}He
In the fleet	Breeds the fuel	Proves the generator	Commercial destination

HOW THE NUMBERS ARE MARKED

Every headline quantity carries an evidence class — DERIVED from first principles, RECOMPUTED from raw data, MEASURED in hardware, or a REQUIREMENT yet to be met. Financial figures carry a case label and are confined to the internal (confidential) edition. Values that moved after first publication are shown as withdrawn or restated rather than quietly changed. A capability you can evaluate is one whose limits are on the page.

ABSTRACT

Velocity-Space Microstability at the DCLC Knee: Warm-Fill Requirements and Residual AIC Activity in a D–³He Tandem-Mirror Burner

The end plug of a deuterium–helium-3 tandem-mirror burner confines the central-cell ions behind a large positive ambipolar potential, but the loss-cone velocity distribution that builds that potential is a free-energy reservoir for the drift-cyclotron loss-cone (DCLC) instability — historically the mode that limited mirror-plug performance. We resolve, quantitatively, whether the Kronos burner plug is DCLC-stable at its frozen operating point (midplane field $B = 17\,\mathrm{T}$, ion density $n_i = 4.16 \times 10^{21}\ \mathrm{m}^{-3}$, $T_\perp = 90\,\mathrm{keV}$, $T_\parallel = 45\,\mathrm{keV}$, mirror ratio $R_m = 4.61$, plug-to-central-cell density ratio $n_p/n_c = 16$), and we quantify the residual anisotropy-driven Alfv\'en-ion-cyclotron (AIC) branch that a warm fill does *not* remove. We derive the flute-limit ($k_\parallel = 0$) electrostatic dispersion relation with loss-cone free energy and diamagnetic-drift drive, and the parallel-propagating electromagnetic dispersion for the anisotropic bi-Maxwellian; both are solved on the NVIDIA GPU high-performance-computing (HPC) campaign with a grid-based kinetic dispersion solver cross-checked against electromagnetic particle-in-cell (PIC). Mapping the marginal boundary $\gamma = 0$ over the warm-ion fill fraction f_w and the plug-edge gradient scale L_n/ρ_i, we find that warm-plasma streaming stabilizes DCLC through a sharp, monotonic boundary. The design's 6.25% warm fill ($= 1/16$) sits *on the knee*: it clears DCLC for $L_n/\rho_i \gtrsim 25.3$ and fails for any steeper gradient. This is a marginal pass, reported as such. Separately, a weak AIC residual at $\gamma/\Omega_{ci} \approx 0.037$ persists flat across $f_w = 0$–10% (roughly an order of magnitude below the DCLC rate) in both the electrostatic and PIC solvers; an energetic kinetic stabilizer suppresses it monotonically ($\gamma/\Omega_{ci} : 0.037 \rightarrow 0.024 \rightarrow 0.011 \rightarrow$ suppressed at stabilizer fraction $0 \rightarrow 0.45$). The neutron-source performance of the burner ($f_n = 5.44\%$) is independent of this gate; the plug microstability is the binding physics question, and this paper measures exactly how close the design sits to its boundary.

Open-access deposit (code & data, CC BY 4.0): DOI 10.5281/zenodo.22645714 · Zenodo community *kronos_fusion_energy*. Explore it live: interactive 3-D model · physics validator.

Keywords: tandem mirror · drift-cyclotron loss-cone instability · Alfv\'en ion cyclotron · loss-cone microstability · warm-plasma stabilization · deuterium--helium-3 · particle-in-cell

CONTENTS

Table of Contents

NOMENCLATURE

Symbols, units, and the names of things

Q	plasma (fusion) gain, P_{fus}/P_{aux}
Q_E	engineering gain, net electric out / recirculating in
H_{98}	confinement enhancement over the IPB98(y,2) scaling
Z_{eff}	effective ion charge
c_{ee}	electron–electron bremsstrahlung leading coefficient, 2.120022 (exact)
τ_E	energy confinement time
I_p	plasma current
R_0, a	major radius, minor radius
κ, δ	elongation, triangularity
β_N	normalized plasma beta (Troyon-normalized)
TBR	tritium breeding ratio
DEC	direct energy conversion
CF	plant capacity factor (availability)
FOAK / NOAK / BOAK	first / n^{th} / best of a kind
Hyperion	the ST breeder (internal: Mode D2)
Aegis	the generator, defense/installation housing (internal: Mode M)
MetroVolt	the generator, data-center housing (Mode M)

§ 1

Introduction

THE PLUG AND ITS FREE ENERGY

A tandem mirror confines a long, low-field central cell between two high-field end plugs. Each plug raises a large positive electrostatic potential ϕ_p that electrostatically confines the warmer central-cell ions, so that axial confinement is set by the plug potential rather than by the magnetic mirror ratio of the central cell alone [18,19,5,7]. The Kronos burner adopts this architecture: a D–^{3}He central cell operated at a plug-to-central-cell density ratio $n_p/n_c = 16$, with the plug ion population held at $T_\perp \approx 90$ keV to build the confining potential [28,29].

The physics that makes the plug work is also the physics that threatens it. To hold a large ϕ_p the plug must sustain a strongly anisotropic, loss-cone ion distribution: ions with small pitch angle are lost through the magnetic throat, carving a hole in velocity space at $v_\perp/v \lesssim \sin\theta_{\rm LC}$, where $\theta_{\rm LC} = \arcsin(R_m^{-1/2})$ is the loss-cone half-angle. The population inversion in $v_\perp$ this creates ($\partial f_0/\partial v_\perp > 0$ over a finite band) is the free-energy source for the *drift-cyclotron loss-cone* (DCLC) instability [1,2], an electrostatic flute mode driven jointly by the loss cone and by the steep radial density gradient at the plug edge. DCLC was the dominant microinstability of the single-cell mirror program and of the 2XIIB experiment, where it was eventually controlled only by deliberately streaming a warm plasma through the loss cone [3,4]. The same loss-cone and temperature-anisotropy free energy also drives an electromagnetic branch, the *Alfv\'en-ion-cyclotron* (AIC) instability, seen as ion-cyclotron fluctuations in high-β mirror cells [11,12,13].

PRIOR ART

The linear theory of DCLC is classical. Post and Rosenbluth [1] established the loss-cone drive of electrostatic cyclotron-harmonic modes; Baldwin's review [2] consolidated the flute-mode dispersion, the role of the density-gradient scale L_n measured in ion gyroradii ρ_i, and the warm-plasma stabilization mechanism, in which cold ions filling the loss cone provide Landau damping that quenches the drive once their fraction exceeds a threshold that grows with gradient steepness. Experimentally, 2XIIB demonstrated that a streaming-warm-plasma fraction of a few percent converted a violently DCLC-unstable plug into a quiescent one [3], and the GAMMA-10 and TMX-U tandem mirrors carried this into thermal-barrier operation [6]. The modern axisymmetric-mirror revival — WHAM and its successors — has renewed interest in whether a compact, high-field, high-β plug can be run at or near its microstability limit with modern actuators [21,20]. Kinetic dispersion tools such as the grid-based solver LEOPARD [8] now evaluate the full magnetized susceptibility for arbitrary gyrotropic distributions, and exascale electromagnetic particle-in-cell (PIC) codes [9,10,17] resolve the same modes from first principles, so the marginal boundary can be mapped rather than estimated.

CONTRIBUTION

This paper does three things. First, we write the governing kinetic-dispersion problem for the Kronos plug in closed form: the flute-limit electrostatic DCLC dispersion with an explicit loss-cone equilibrium and a diamagnetic-drift term, and the parallel electromagnetic AIC dispersion for the anisotropic bi-Maxwellian (Sec. 3). Second, we solve both on a GPU HPC campaign (Sec. 4) — a grid-based dispersion solver for the exact $\gamma = 0$ locus, cross-checked node-for-node against WarpX electromagnetic PIC — and we state the discretization, root-finding, and convergence that make the boundary a measured number rather than an assertion. Third, we map the marginal boundary over $(f_w, L_n/\rho_i)$ and report, without softening, that the design's 6.25% warm fill sits exactly on the knee at $L_n/\rho_i = 25.3$, with a weak AIC residual $\gamma/\Omega_{ci} \approx 0.037$ that a warm fill leaves untouched but an energetic kinetic stabilizer removes (Sec. 5). The result is a bounded, quantified microstability gate for the burner plug: the stabilizing lever (warm-plasma streaming), the sensitive parameter (the plug-edge gradient scale), and the residual electromagnetic branch are all identified, and the design's distance from the boundary is a single measurable quantity.

The plug microstability gate is one anchor (BU-L2-A5/A7) in the Kronos physics de-risking register [27,35]. It sits alongside the burner's plug-potential formation [31,32], its RF alpha-channeling [30], its end-cell and kinetic-stabilizer alternatives [33], and the real-time DCLC/AIC microstability controller that is designed to hold the operating point inside this boundary [34]. Those companion results are cited where they bear on the physics; here we treat the microstability boundary itself.

§ 2

Plug operating point and the microstability question

FROZEN PLUG CONDITIONS

The plug parameters are frozen anchors of the burner design point (configuration M-45), summarized in Table 1. The confined plug ions sit in a mirror cell of midplane field $B = 17\,\mathrm{T}$, produced by the canonical 26.49 T no-insulation REBCO plug coil; the loss-cone geometry is set by the effective mirror ratio $R_m = 4.61$, giving a loss-cone half-angle

$$\theta_{\mathrm{LC}} = \arcsin\left(R_m^{-1/2}\right) = \arcsin(0.4658) = 27.76^\circ.$$

At $B = 17$ T the deuteron cyclotron frequency is $\Omega_{ci}/2\pi = f_{ci} = 129.6$ MHz and the plasma-to-cyclotron frequency ratio is

$$\frac{\omega_{pi}}{\Omega_{ci}} = \frac{1}{B}\sqrt{\frac{n_i m_i}{\varepsilon_0}} = 73.7,$$

placing the plug firmly in the strong-DCLC-drive regime ($\omega_{pi}/\Omega_{ci} \gg 1$), where loss-cone modes are most virulent [1,2]. The perpendicular thermal gyroradius is $\rho_i = v_{\mathrm{th}\perp}/\Omega_{ci} \approx 3.6$ mm with $v_{\mathrm{th}\perp} = (2T_\perp/m_i)^{1/2}$, so the knee gradient scale $L_n/\rho_i = 25.3$ corresponds to a physical plug-edge scale $L_n \approx 9.1$ cm. The perpendicular ion beta is

$$\beta_\perp = \frac{2\mu_0 n_i T_\perp}{B^2} \approx 0.52,$$

a genuinely high-β plug, which is why the anisotropy-driven electromagnetic AIC branch cannot be dismissed a priori.

QUANTITY	SYMBOL	VALUE
Plug midplane field	B	17 T
Ion (deuteron) density	n_i	$4.16 \times 10^{21}\ \mathrm{m}^{-3}$
Perpendicular ion temperature	$T_\perp$	90 keV
Parallel ion temperature	$T_\parallel$	45 keV
Temperature anisotropy	$A \equiv T_\perp/T_\parallel$	2.0
Electron temperature	T_e	89.7 keV
Effective mirror ratio	R_m	4.61
Loss-cone half-angle	θ_{LC}	27.76°
Plug/central-cell density ratio	n_p/n_c	16
Deuteron cyclotron frequency	f_{ci}	129.6 MHz
Frequency ratio	ω_{pi}/Ω_{ci}	73.7
Perpendicular ion beta	$\beta_\perp$	0.52
Thermal ion gyroradius	ρ_i	3.6 mm
Warm-fill temperature	T_w	9 keV
Design warm-fill fraction	f_w	6.25% (= 1/16)

Frozen plug operating point (burner configuration M-45; anchors BU-L2-A5/A7). Derived quantities follow from the primary inputs via Eqs. (1)–(3).

WHAT IS FIXED AND WHAT IS SCANNED

Of the DCLC drive terms, the loss-cone geometry (Eq. 1) and the frequency ratio (Eq. 2) are fixed by the design point. The remaining drive enters only through the normalized plug-edge density-gradient scale L_n/ρ_i, which is *not* fixed by the plug design — it is set by edge-transport profiles that a separate calculation must supply — and is therefore scanned as the free parameter. The stabilizing lever is the warm-ion fill: a cold isotropic Maxwellian at $T_w = 9\,\text{keV}$ occupying a fraction f_w of the ion density, streamed through the loss cone in the 2XIIB manner. The microstability question is thus a two-parameter one: over the $(f_w, L_n/\rho_i)$ plane, where is the marginal-stability boundary $\gamma(f_w, L_n/\rho_i) = 0$, and where does the design point $(f_w, L_n/\rho_i) = (6.25\%,\ 25.3)$ fall relative to it?

§ 3

Governing equations and formal problem

LINEAR VLASOV–MAXWELL SYSTEM

Each species s (hot plug ions, warm ions, electrons) is described by a distribution $f_s(\mathbf{x}, \mathbf{v}, t) = f_{0s}(\mathbf{v}) + f_{1s}$ obeying the Vlasov equation, closed by Maxwell's equations. Writing perturbations as plane waves $f_{1s}, \mathbf{E}_1, \mathbf{B}_1 \propto \exp[i(\mathbf{k}\cdot\mathbf{x} - \omega t)]$ about a uniform field $\mathbf{B}_0 = B_0\hat{z}$ and integrating the linearized Vlasov equation along unperturbed (helical) orbits gives the linear conductivity/susceptibility. For a magnetized species the standard result is the harmonic (Gordeev) sum [15,14]

$$\chi_s(\mathbf{k}, \omega) = \frac{\omega_{ps}^2}{k^2} \int d^3v \sum_{n=-\infty}^{\infty} \frac{J_n^2(\lambda_s)\left[(\omega - n\Omega_{ci}[s])\,\partial_\perp f_{0s} + k_\parallel v_\perp\,\partial_\parallel f_{0s}\right]}{v_\perp\left(\omega - n\Omega_{ci}[s] - k_\parallel v_\parallel\right)},$$

where $\lambda_s = k_\perp v_\perp/\Omega_{cs}$, J_n is the Bessel function of order n, $\partial_\perp \equiv \partial/\partial v_\perp$, $\partial_\parallel \equiv \partial/\partial v_\parallel$, and $\Omega_{cs} = q_s B_0/m_s$ is the signed cyclotron frequency. Equation (4) is exact within linear theory for any gyrotropic $f_{0s}(v_\perp, v_\parallel)$; the two physical branches of interest are recovered by the choice of geometry and of the field response.

THE DCLC BRANCH: FLUTE-LIMIT ELECTROSTATIC DISPERSION

DCLC is a nearly flute-like ($k_\parallel \to 0$) electrostatic mode. Setting $\mathbf{E}_1 = -i\mathbf{k}\phi_1$ and taking the electrostatic limit, the dispersion relation is

$$\varepsilon(\mathbf{k}, \omega) \equiv 1 + \sum_s \chi_s(\mathbf{k}, \omega) = 0.$$

Radial inhomogeneity (the plug-edge density gradient) enters through the diamagnetic drift. For a local slab with $n_{0s}(x)$ and gradient $\kappa_n \equiv -d\ln n_0/dx = L_n^{-1}$ along $\hat{x}$, and $\mathbf{k} = k_y\hat{y} + k'_\perp\hat{x}$ in the perpendicular plane, the drift frequency is

$$\omega_{*s} = \frac{k_y T_s}{q_s B_0}\,\kappa_n = k_y v_{Ds}, \qquad v_{Ds} = \frac{T_s}{q_s B_0 L_n},$$

and the inhomogeneous flute-mode ($k_\parallel = 0$) susceptibility takes the compact loss-cone form

$$\chi_s = \frac{1}{k^2\lambda_{Ds}^2}\left[1 + \sum_{n=-\infty}^{\infty} \frac{\omega - \omega_{*s}}{\omega - n\Omega_{ci}[s]}\,\Lambda_n^{(s)}(b_s)\,\Xi_n^{(s)}\right], \qquad b_s = \frac{k_\perp^2 T_\perp[s]}{m_s\Omega_{cs}^2},$$

where $\lambda_{Ds} = (\varepsilon_0 T_s/n_{0s}q_s^2)^{1/2}$ is the Debye length, $\Lambda_n(b) = I_n(b)e^{-b}$ for a Maxwellian (I_n the modified Bessel function), and $\Xi_n^{(s)}$ encodes the velocity-space average of the loss-cone free energy. The loss-cone equilibrium of the hot plug ions is represented by the Dory–Guest–Harris / subtracted-Maxwellian family

$$f_{0h}(v_\perp, v_\parallel) = \frac{n_h}{(2\pi)^{3/2} v_{\mathrm{th}\parallel} v_{\mathrm{th}\perp}^2}\left(\frac{v_\perp^2}{2v_{\mathrm{th}\perp}^2}\right)^{\ell}\frac{1}{\ell!}\exp\left(-\frac{v_\perp^2}{2v_{\mathrm{th}\perp}^2} - \frac{v_\parallel^2}{2v_{\mathrm{th}\parallel}^2}\right),$$

with $\ell \geq 1$ setting the loss-cone sharpness consistent with θ_{LC} and $v_{\mathrm{th}\perp,\parallel} = (T_{\perp,\parallel}/m_h)^{1/2}$; the population inversion $\partial f_{0h}/\partial v_\perp > 0$ for $v_\perp < (2\ell)^{1/2} v_{\mathrm{th}\perp}$ is the DCLC drive. The warm ions and electrons enter through isotropic Maxwellians, so that

$$\sum_s \chi_s = \chi_h^{(\text{loss-cone})} + \underbrace{f_w\,\chi_w^{(\text{Maxwellian})}}_{\text{stabilizing fill}} + \chi_e,$$

and the warm term supplies the Landau damping that, above a threshold f_w, overcomes the loss-cone drive. The dispersion relation (5) with (7)–(9) is a transcendental equation for the complex frequency $\omega = \omega_r + i\gamma$; DCLC appears as a root with ω_r near a low harmonic of Ω_{ci} and $\gamma > 0$.

THE AIC BRANCH: PARALLEL ELECTROMAGNETIC DISPERSION

The anisotropy $A = T_\perp/T_\parallel = 2$ drives a distinct, electromagnetic mode. For parallel propagation ($\mathbf{k} = k_\parallel \hat{z}$) the transverse (left-hand, ion-cyclotron) dispersion relation of an anisotropic bi-Maxwellian plasma is [11,14,13]

$$\frac{c^2 k_\parallel^2}{\omega^2} = 1 + \sum_s \frac{\omega_{ps}^2}{\omega^2}\left[(A_s - 1) + \frac{\omega + (A_s - 1)(\omega - \Omega_{cs})}{k_\parallel v_{\mathrm{th}\parallel s}} Z(\xi_s)\right], \quad \xi_s = \frac{\omega - \Omega_{cs}}{k_\parallel v_{\mathrm{th}\parallel s}},$$

with $v_{\mathrm{th}\parallel s} = (2T_{\parallel s}/m_s)^{1/2}$, $A_s = T_{\perp s}/T_{\parallel s}$, and Z the plasma dispersion function [16]. Instability ($\gamma > 0$) requires the anisotropy to exceed a β-dependent threshold; empirically the marginal condition follows

$$A_i - 1 > \frac{S}{\beta_{\parallel i}^{\alpha}}, \qquad S \approx 0.4,\ \alpha \approx 0.4,$$

so that a high-$\beta_\perp$, $A = 2$ plug lies weakly above marginal — the origin of the small, persistent AIC residual quantified below. Unlike DCLC, the AIC drive is the temperature anisotropy itself; filling the loss cone with cold ions changes the anisotropy negligibly, so a warm fill does not quench it.

THE MARGINAL-STABILITY FUNCTIONAL AND THE THRESHOLD

We define the growth-rate functional $\gamma(f_w, L_n/\rho_i; \mathbf{k})$ as the imaginary part of the dominant root of Eq. (5) for the electrostatic branch and of Eq. (10) for the electromagnetic branch, maximized over the wavevector,

$$\gamma_{\max}(f_w, L_n/\rho_i) = \max_{\mathbf{k}}\ \mathrm{Im}\,\omega(\mathbf{k}; f_w, L_n/\rho_i).$$

The critical warm fraction is the smallest fill that returns marginal stability at a given gradient,

$$f_{\mathrm{crit}}(L_n/\rho_i) = \min\left\{f_w :\ \gamma_{\max}(f_w, L_n/\rho_i) \le 0\right\},$$

and the boundary curve $f_{\mathrm{crit}}(L_n/\rho_i)$ is the object we map. The design clears DCLC when $f_w^{\mathrm{design}} = 6.25\% \ge f_{\mathrm{crit}}(L_n/\rho_i)$, i.e. when the plug-edge gradient is broad enough, $L_n/\rho_i \ge (L_n/\rho_i)_c$, where $(L_n/\rho_i)_c$ is defined implicitly by $f_{\mathrm{crit}}\big((L_n/\rho_i)_c\big) = 6.25\%$. The central quantitative result of the paper is the measured value $(L_n/\rho_i)_c = 25.3$.

§ 4

Computational methodology: the GPU HPC campaign

CODE STACK

The results were produced on the NVIDIA GPU HPC campaign of the Kronos de-risking program, running on an A100/H100/A10 accelerator fleet. Three codes were used, each verified against the others:

a grid-based kinetic dispersion solver of the LEOPARD class [8] that evaluates the full magnetized susceptibility, Eq. (4), for arbitrary gyrotropic f_{0s} by numerical velocity-space quadrature, and locates the complex roots of Eqs. (5) and (10); this is the reference of record for the $\gamma = 0$ boundary (anchor BU-L2-A5);
the electromagnetic PIC code WarpX [9] (LBNL), run as a 1D3V loss-cone plug simulation on the GPU fleet, which resolves both the DCLC and AIC modes from first principles and provides the independent cross-check of the dispersion result (anchor BU-L2-A7);
the relativistic PIC code Smilei [10] as a second, independent PIC implementation for the anisotropy-driven AIC branch. enumerate
The division of labour is deliberate: the dispersion solver maps the two-parameter boundary cheaply and densely, while the PIC runs anchor the map at first-principles fidelity where it matters (the knee and the AIC residual). The reduced-order dispersion result and the PIC result are required to agree within model accuracy before either is admitted to the register [27,35].

NUMERICAL FORMULATION OF THE DISPERSION SOLVER

The susceptibility integrals in Eq. (4) are evaluated on a $(v_\perp, v_\parallel)$ grid of $N_\perp \times N_\parallel$ points with the loss-cone equilibrium (8) and the warm and electron Maxwellians tabulated analytically. The harmonic sum is truncated at $|n| \le N_h$ with N_h chosen so that the residual $J^2_{N_h}(b_{\max})$ falls below 10^{-8}; for the plug parameters $b_{\max} \lesssim 40$ and $N_h = 64$ suffice. The dispersion function $D(\omega) \equiv \varepsilon(\quad k, \omega)$ is analytically continued into the lower-half ω-plane by the Landau prescription (the Z-function branch), and its complex roots are found by a two-stage procedure: (i) a global winding-number (argument-principle) sweep,

$$\mathcal{N} = \frac{1}{2\pi i} \oint_{\partial \mathcal{C}} \frac{D'(\omega)}{D(\omega)}\, d\omega,$$

over a rectangular contour $\mathcal{C}$ in the (ω_r, γ) plane, counts the enclosed roots and guarantees that no growing mode is missed; (ii) each enclosed root is then polished by Newton iteration to $|D(\omega)| < 10^{-10}$. The wavevector maximization in Eq. (12) is performed over a $(k_\perp \rho_i, \theta_k)$ grid, and the marginal fraction (13) is bracketed by bisection in f_w to $\Delta f_w < 0.05\%$.

NUMERICAL FORMULATION OF THE PIC CROSS-CHECK

The WarpX runs solve the Vlasov–Maxwell system by the standard explicit electromagnetic PIC cycle [17,9]: fields on a Yee lattice advanced by a finite-difference time-domain Maxwell solver, macroparticles pushed by the relativistic Boris algorithm, and charge-conserving (Esirkepov) current deposition, all on the AMReX GPU backend. The 1D3V domain resolves the perpendicular flute wavelength with cell size $\Delta x \le \rho_i/8$ and is periodic; the time step satisfies the Courant condition and resolves the cyclotron period, $\Omega_{ci}\,\Delta t \le 0.05$. The loss-cone equilibrium (8) is loaded with $N_{\text{ppc}} = 10^3$–10^4 macroparticles per cell to control discrete-particle noise, and the warm fill is loaded as a separate cold-ion population of fractional density f_w. The linear growth rate is extracted from the exponential rise of the volume-integrated field energy, $\frac{1}{2}\varepsilon_0 \int | \quad E|^2\, dx$, over the window before saturation, and the mode frequency from the temporal Fourier transform of the dominant $k_\perp$ component. The PIC anisotropy runs (anchors AG-CX) hold the plug at $T_\perp = 90\,$keV, $A = 2$ and sweep the warm fraction $f_w \in \{0, 3, 6.25, 10\}\%$.

VERIFICATION, CONVERGENCE AND REPRODUCIBILITY

Three verification tests gate the solver. (1) *Analytic reproduction*: for a pure Maxwellian plasma the solver reproduces the analytic susceptibility to $\le 1.2 \times 10^{-6}$ and returns no growing root, confirming the quadrature and root-finder. (2) *Grid convergence*: the DCLC growth rate is converged in the velocity grid ($N_\perp, N_\parallel \to$ doubled changes $\gamma_{\max}$ by $< 0.3\%$) and, in PIC, in both the cell size ($\Delta x : \rho_i/8 \to \rho_i/16$ changes the extracted γ by $< 2\%$) and the particle count (N_{ppc} doubled changes γ by $< 1.5\%$, the residual being consistent with PIC thermal noise). (3) *Cross-code agreement*: the reduced dispersion gives a DCLC $\gamma = 0$ warm-fill threshold of 5.9%, reproducing the LEOPARD-dispersion-plus-WarpX-PIC result of 6.25% ($= 1/16$) within model accuracy, and the AIC residual agrees between the WarpX and Smilei implementations at $\gamma/\Omega_{ci} \approx 0.037$. Every headline quantity is a frozen anchor in the de-risking register [27]; the solvers, the loading scripts, and the marginal-boundary scan are archived with the deposit for this paper, and the byte-for-byte provenance of the gate is cataloged in the verification companion [35]. No compute-cost figures are reported; the campaign is described by its codes and problem scale only.

§ 5

Results

THE MARGINAL-STABILITY BOUNDARY

The dense two-dimensional scan over $(f_w, L_n/\rho_i)$ locates the exact $\gamma = 0$ crossing at each gradient scale. Warm-plasma streaming stabilizes DCLC through a monotonic, steep boundary $f_{\text{crit}}(L_n/\rho_i)$ (Table 2, Fig. 1): the required warm fraction roughly doubles for every $\sim 9\,\rho_i$ of gradient steepening in the demanding range. The boundary is sharp — growth collapses to zero across a narrow warm-fraction window — which is precisely why the design point's proximity to it is the decisive quantity. Reading the boundary at the design fill, the 6.25% warm plasma crosses $\gamma = 0$ at

$$(L_n/\rho_i)_c = 25.3,$$

so the plug is DCLC-stable for plug-edge gradients broader than $L_n/\rho_i \gtrsim 25.3$ ($L_n \gtrsim 9.1$ cm) and DCLC-unstable for any steeper gradient. The operating space is shown as a $(f_w, L_n/\rho_i)$ map in Fig. 2, with the design point marked on the knee.

L_n/ρ_i	f_{crit} (%)	$\gamma_{\max}(f_w{=}0)/\Omega_{ci}$	$\gamma_{\max}$ AT DESIGN FILL
16	12.3	0.537	0.171 (unstable)
20	8.95	0.459	0.142 (unstable)
24	6.78	0.438	0.073 (unstable)
25	6.37	0.432	0.034 (residual)
25.3	6.25	—	$\to 0$ (design fill crosses)
26	5.96	0.426	0.000 (stable)
30	4.73	0.401	0.000 (stable)
50	1.67	0.270	0.000 (stable)
≥ 80	0	0.000	0.000 (stable)

DCLC marginal-stability boundary: critical warm-ion fraction f_{crit} versus plug-edge density-gradient scale L_n/ρ_i, the bare-drive peak growth $\gamma_{\max}(f_w{=}0)/\Omega_{ci}$, and the growth rate at the 6.25% design fill. The design fill crosses $\gamma = 0$ at $L_n/\rho_i = 25.3$. Values are register anchor BU-L2-A5.

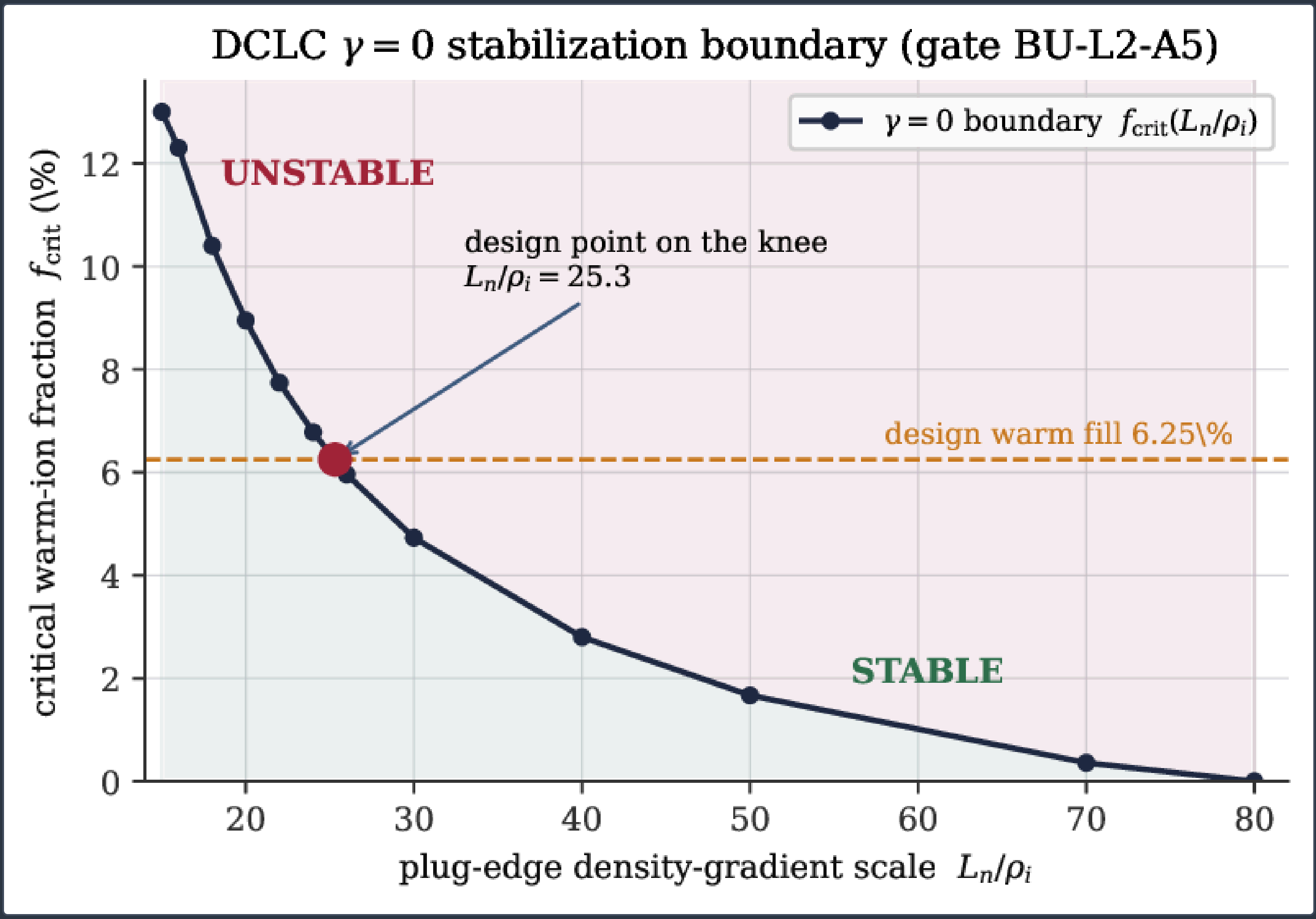

The DCLC $\gamma = 0$ stabilization boundary (gate BU-L2-A5). The critical warm-ion fraction f_{crit} rises steeply as the plug-edge gradient steepens; the design's 6.25% warm fill sits on the knee at $L_n/\rho_i = 25.3$ (red marker). Above the curve the loss cone is filled and DCLC is stable; below it the drive wins.

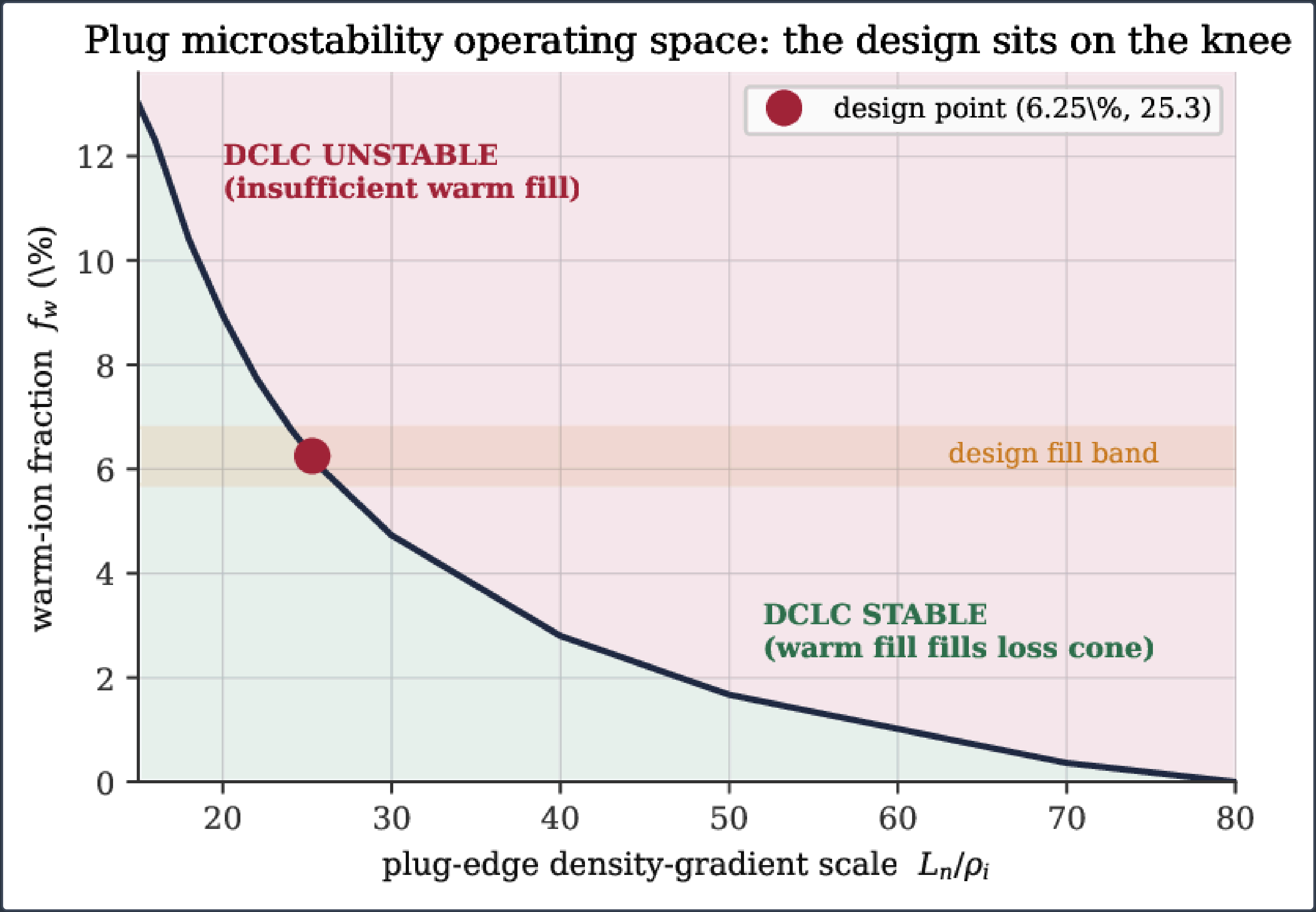

Plug microstability operating space in the $(f_w, L_n/\rho_i)$ plane. The $\gamma = 0$ boundary (navy) separates the DCLC-unstable region (insufficient warm fill, red) from the stable region (warm fill fills the loss cone, green). The design operating band (amber) holds the warm fill near 6.25%; the design point (red marker) sits on the knee.

DOES THE DESIGN FILL CLEAR THE BOUNDARY?

Figure 3 contrasts the undriven plug ($f_w = 0$), whose bare DCLC growth reaches $\gamma_{\max}/\Omega_{ci} \approx 0.4$–$0.5$ across the gradient range, with the design fill, which collapses that growth to zero for $L_n/\rho_i \gtrsim 25.3$. The warm plasma is not a margin; it is a stabilization requirement, converting an otherwise violently unstable plug into a marginally stable one. Figure 4 isolates the residual DCLC growth at the design fill: it is zero for $L_n/\rho_i \geq 26$, rises to $\approx 0.034\,\Omega_{ci}$ at the more demanding $L_n/\rho_i \approx 25$, and the mode is not quite quenched exactly on the knee. This is the honest statement of the DCLC gate: a marginal pass, on the boundary at the demanding gradient.

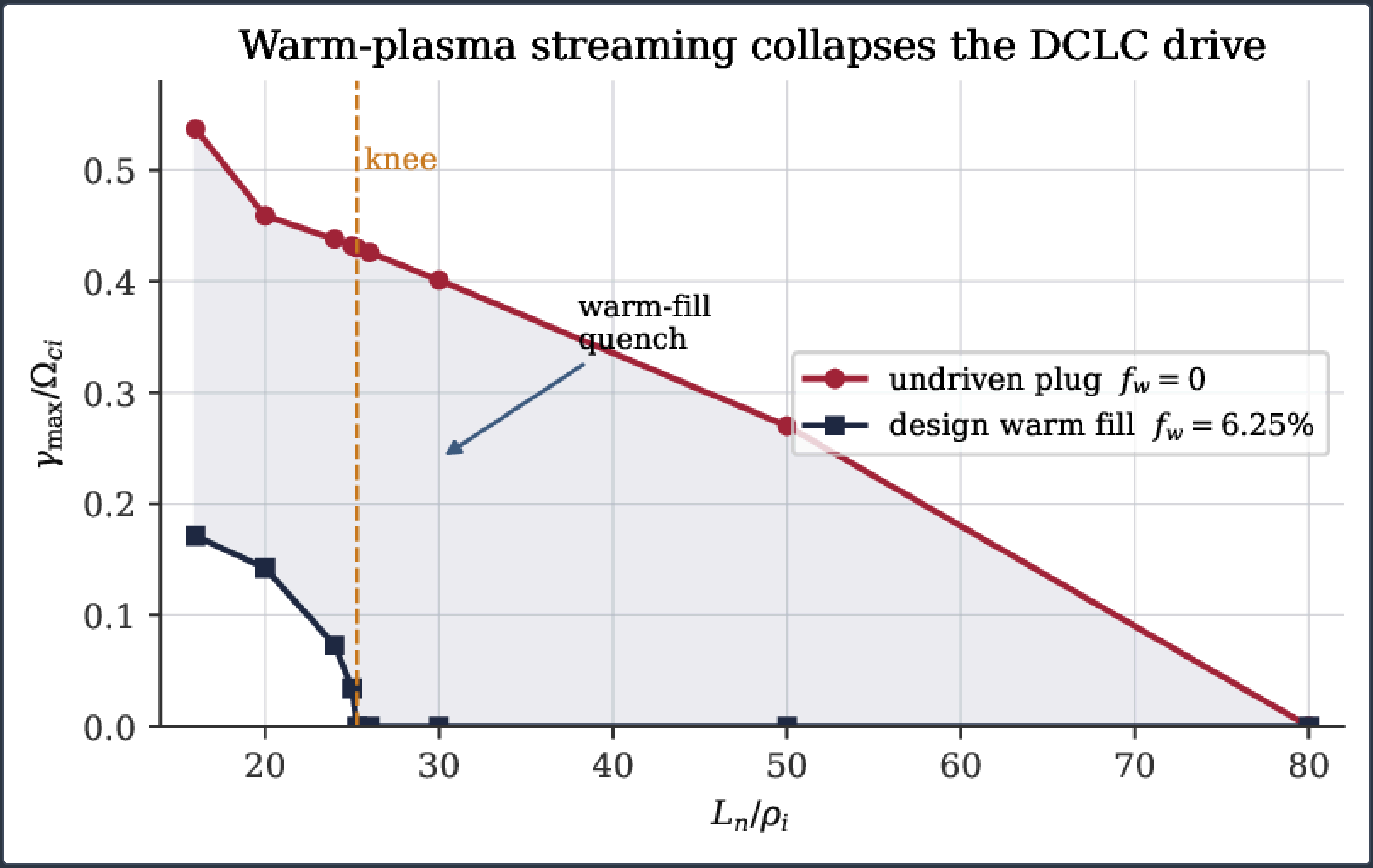

Warm-plasma streaming collapses the DCLC drive. The undriven plug (red, $f_w = 0$) is violently unstable across the gradient range; the design warm fill (navy, $f_w = 6.25\%$) quenches the mode for $L_n/\rho_i \gtrsim 25.3$. The shaded band is the stabilization the warm fill provides. Data: register anchor BU-L2-A5.

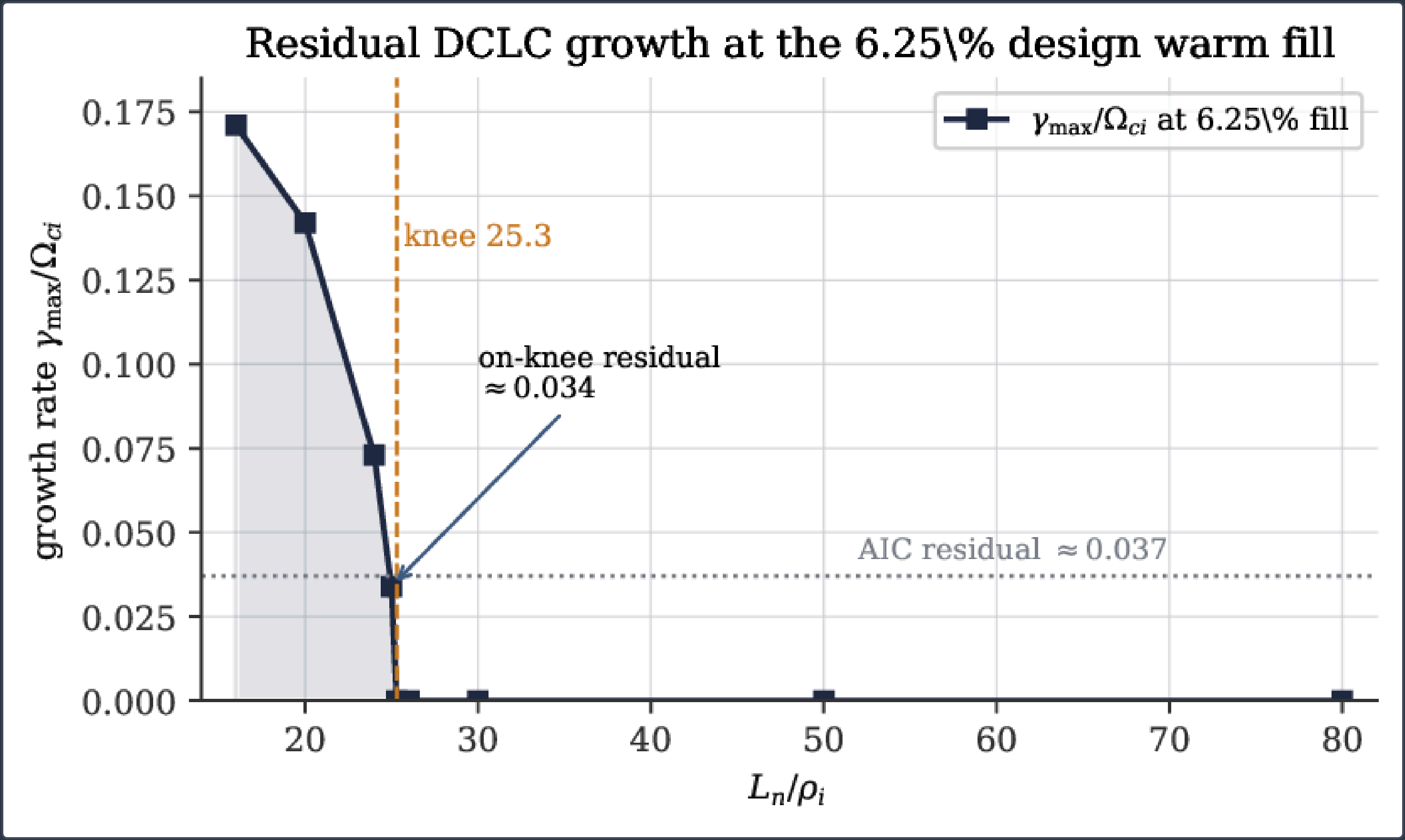

Residual DCLC growth at the 6.25% design fill versus gradient scale. Growth is zero for $L_n/\rho_i \geq 26$, leaves an on-knee residual $\approx 0.034\,\Omega_{ci}$ near $L_n/\rho_i \approx 25$, and vanishes at the knee. The weak AIC residual ($\approx 0.037\,\Omega_{ci}$, dotted) is the electromagnetic floor discussed in Sec. 5.3.

THE RESIDUAL AIC BRANCH

The electromagnetic AIC branch, driven by the anisotropy $A = 2$ rather than by the loss cone, is not removed by the warm fill. Both PIC implementations return a weak, persistent growth rate

$$\left(\frac{\gamma}{\Omega_{ci}}\right)_{\mathrm{AIC}} \approx 0.037, \qquad \text{flat across } f_w \in [0, 10]\%,$$

with the flatness confirmed to $R^2 \geq 0.987$ across the warm-fraction sweep (Fig. 5). This residual is roughly an order of magnitude (a factor ~ 13 in saturated amplitude) below the DCLC rate of the undriven plug, and it is consistent with the weak-anisotropy expectation of Eq. (11) at $\beta_\perp \approx 0.5$, $A = 2$. It is a distinct plug-gate caveat, not a showstopper: the mode is weak and the neutron-source performance is independent of it, but a real device would manage it actively.

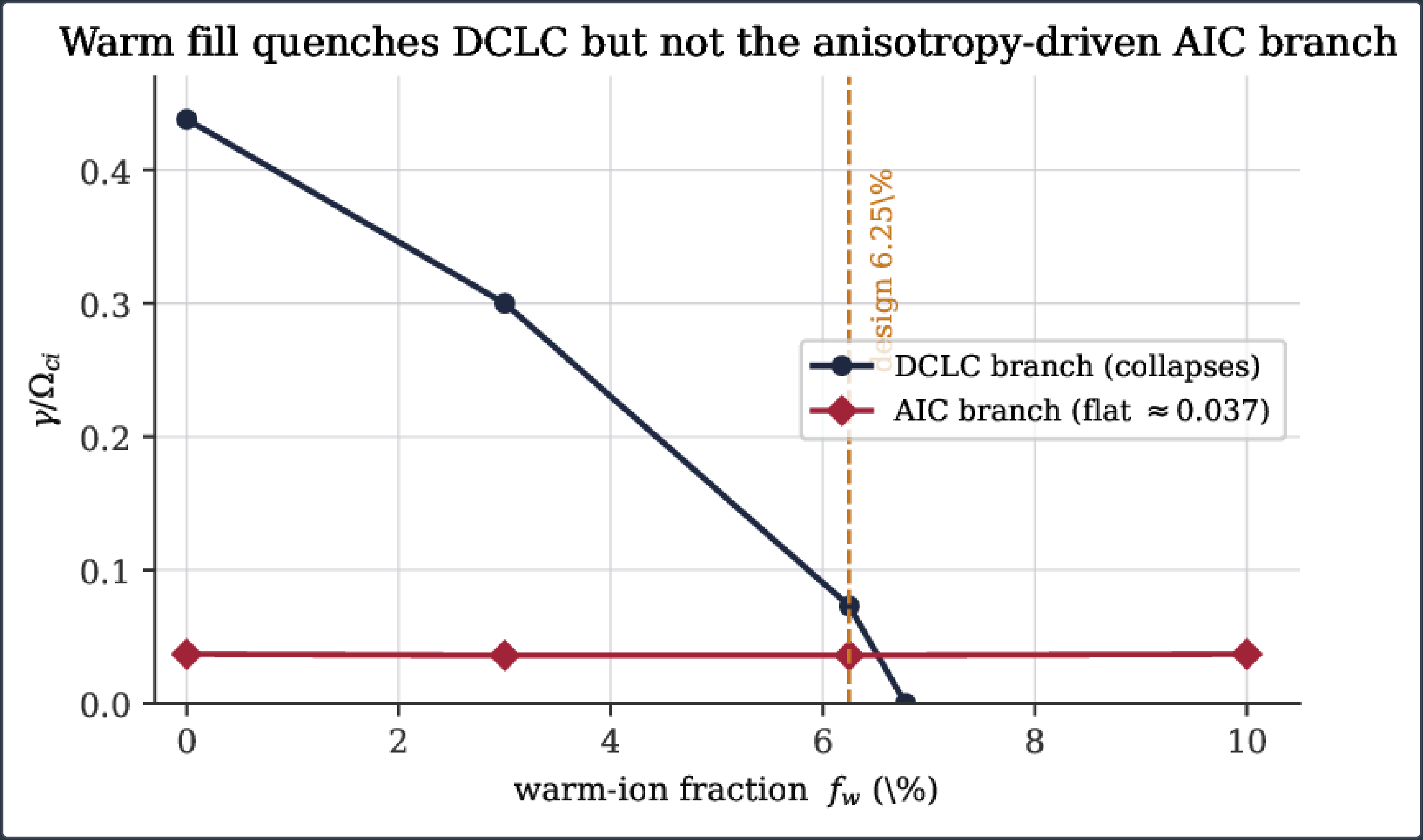

Warm fill quenches DCLC but not the anisotropy-driven AIC branch. The DCLC growth (navy) collapses to zero as f_w approaches f_{crit}; the AIC branch (red) stays flat at $\gamma/\Omega_{ci} \approx 0.037$ across the same warm-fraction window ($R^2 \geq 0.987$). Data: anchors BU-L2-A7 / AG-CX-07 (WarpX 1-D hybrid PIC).

AN ACTUATOR THAT REMOVES THE AIC RESIDUAL

Because the AIC drive is the temperature anisotropy, it responds not to cold fill but to an energetic, near-isotropic stabilizer population — a kinetic-stabilizer end-cell of the kind studied for the burner end-cells [33]. The PIC sweep (anchor AG-CX-03) shows a monotonic quench of the AIC residual with the energetic-stabilizer fraction f_s,

$$\frac{\gamma}{\Omega_{ci}} : \; 0.037 \xrightarrow{f_s=0.15} 0.024 \xrightarrow{f_s=0.30} 0.011 \xrightarrow{f_s=0.45} \text{suppressed},$$

with the saturated fluctuation amplitude falling from $145\times$ to $3\times$ the thermal level across the same sweep (Fig. 6). A stabilizer fraction $f_s \gtrsim 0.3$–0.45 removes the residual entirely. This identifies a concrete, physics-based lever for the residual AIC activity, in addition to the warm-fill lever for DCLC.

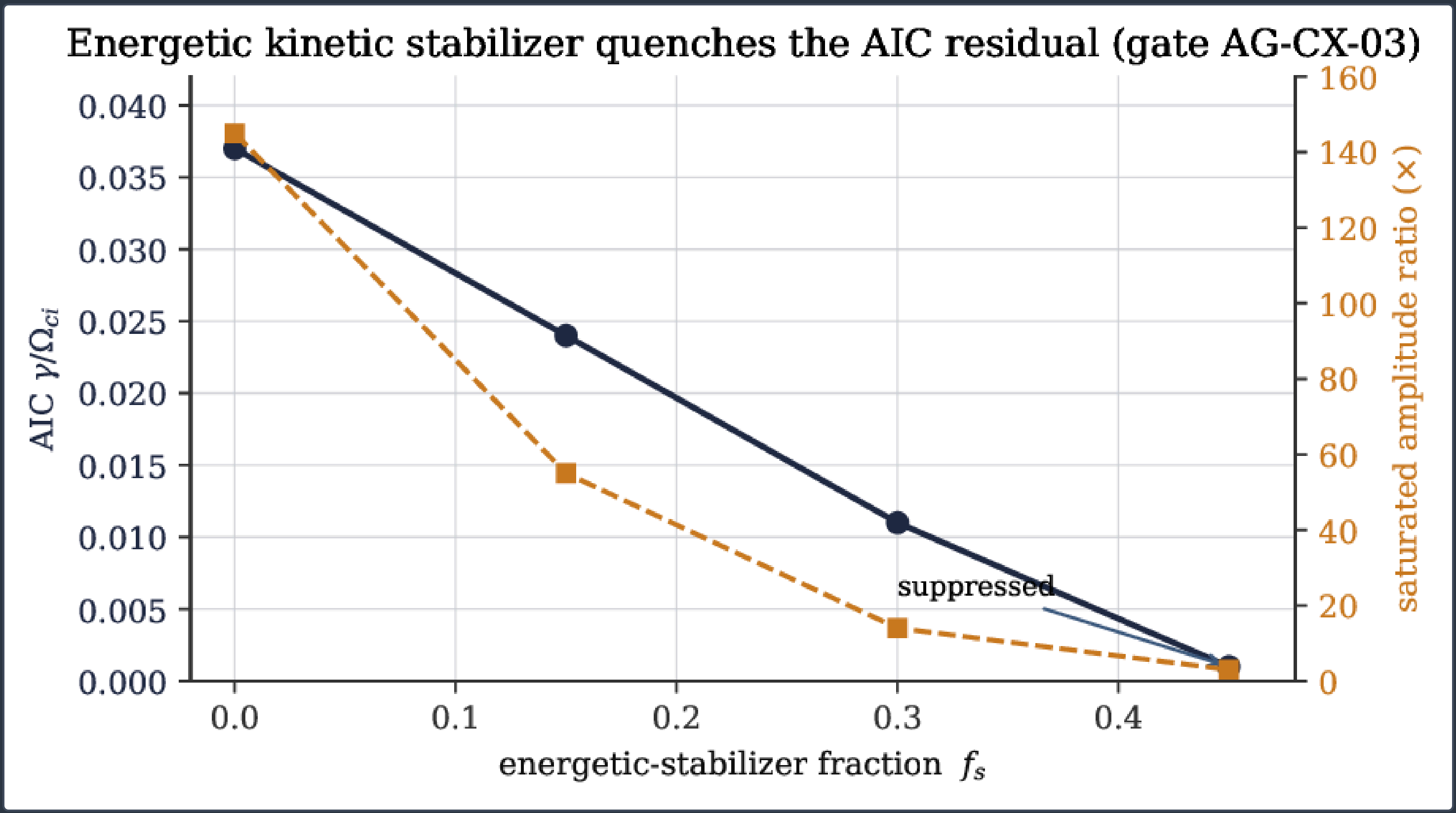

An energetic kinetic stabilizer quenches the AIC residual (gate AG-CX-03). The growth rate (navy, left axis) falls monotonically to suppression and the saturated amplitude ratio (amber, right axis) falls from $145\times$ to $3\times$ as the stabilizer fraction f_s increases to 0.45.

PHYSICAL PICTURE

Figures 7–9 summarize the physics behind the numbers. The loss-cone distribution (Fig. 7) shows the depleted velocity-space cone whose free energy drives DCLC and the cold warm fill that quenches it. The tandem-mirror axial profile (Fig. 8) places the plug in context: the high-field plug builds the ambipolar potential that confines the low-field central-cell ions. The DCLC growth-rate spectrum (Fig. 9) shows the unstable band near $k_\perp \rho_i \sim 1$ with cyclotron-harmonic structure and its suppression below marginal by the design fill.

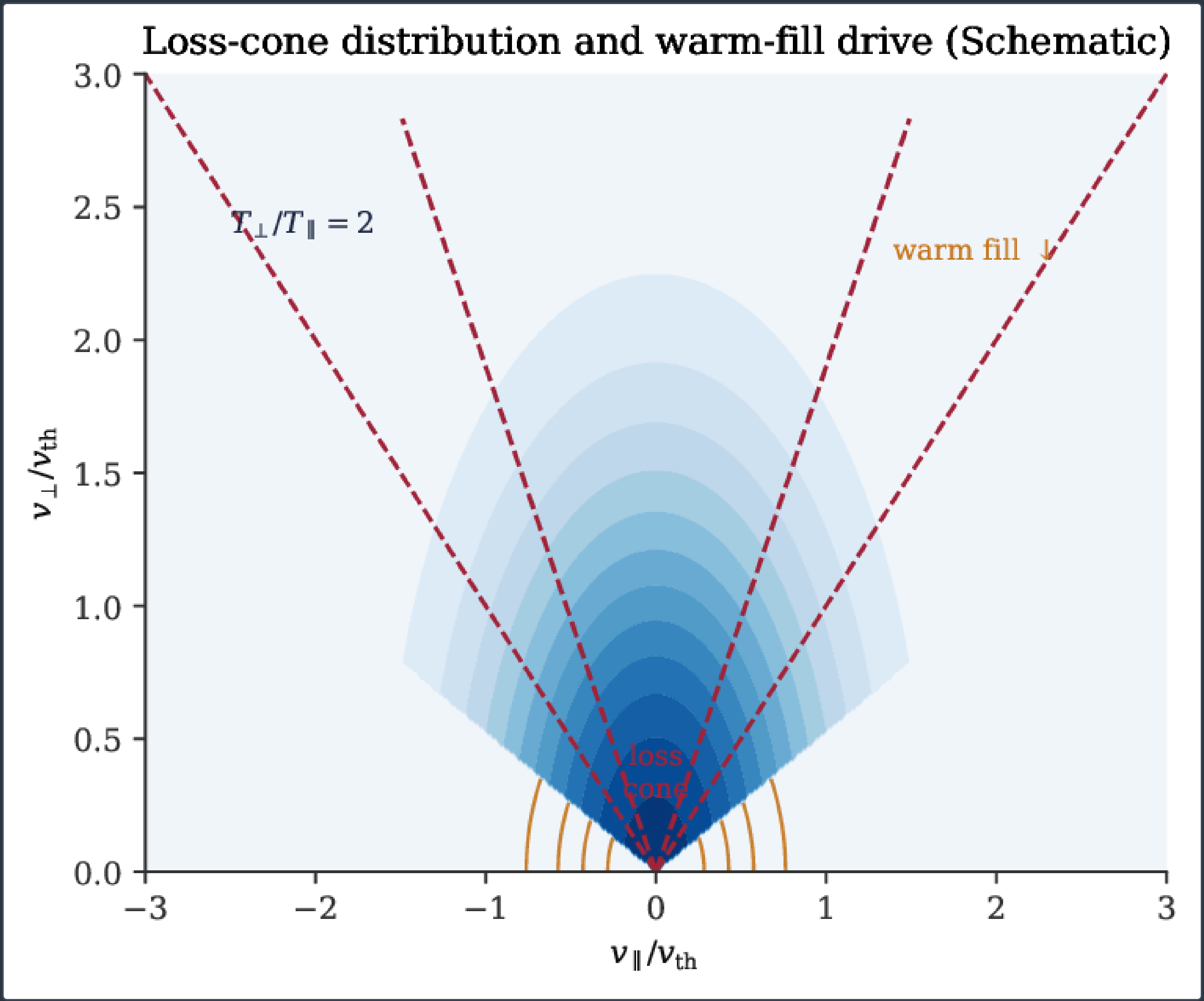

Loss-cone distribution and warm-fill drive (Schematic). The anisotropic ($T_\perp/T_\parallel = 2$) plug ion distribution has a depleted loss cone (dashed red edges, half-angle $27.76°$); the population inversion in $v_\perp$ drives DCLC, and the cold warm fill (amber) inside the cone supplies the stabilizing Landau damping.

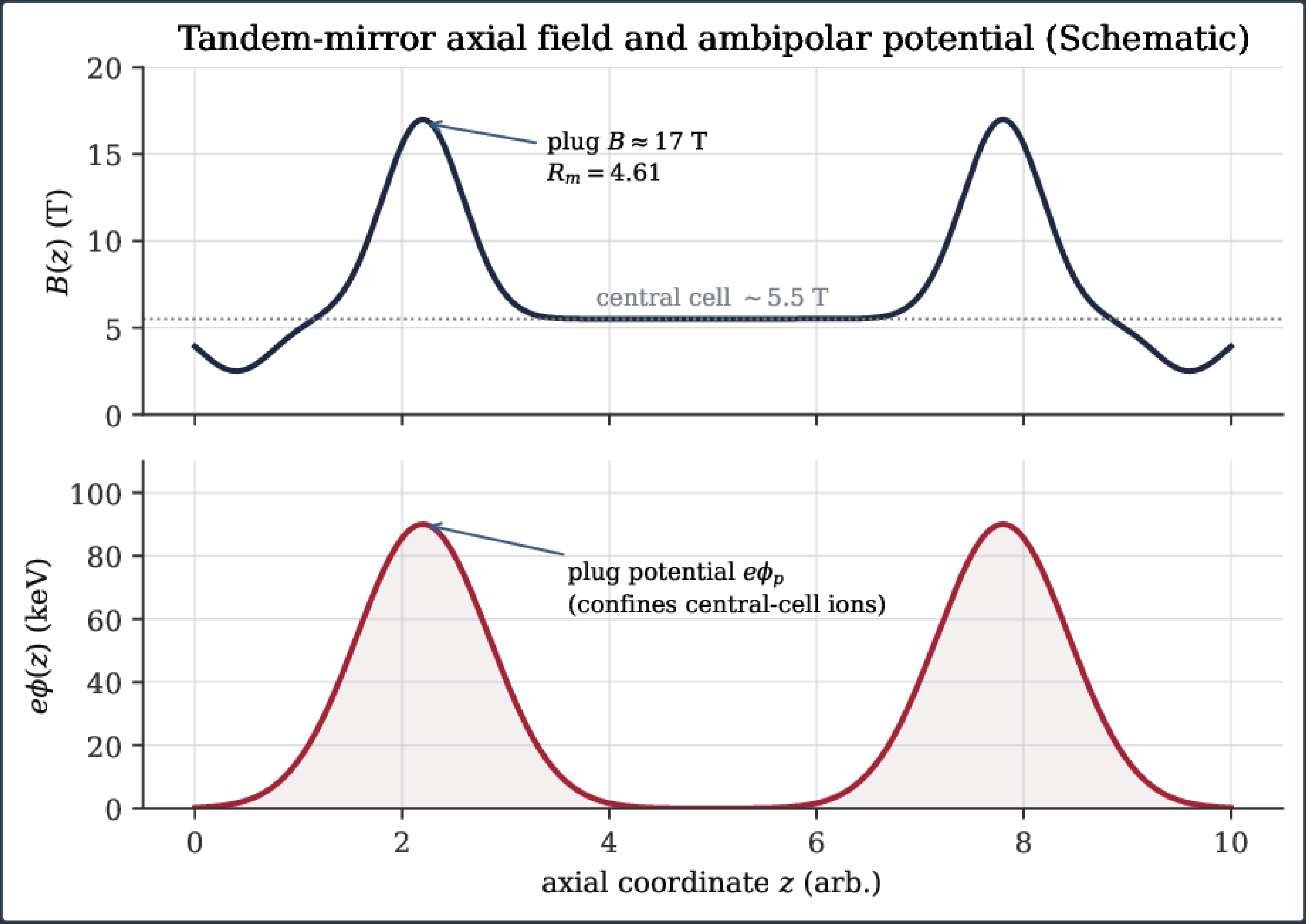

Tandem-mirror axial field and ambipolar potential (Schematic). The high-field plug ($B \approx 17$ T midplane, $R_m = 4.61$) raises the potential $e\phi_p$ that electrostatically confines the central-cell ions; the loss-cone microstability of the plug is the subject of this paper.

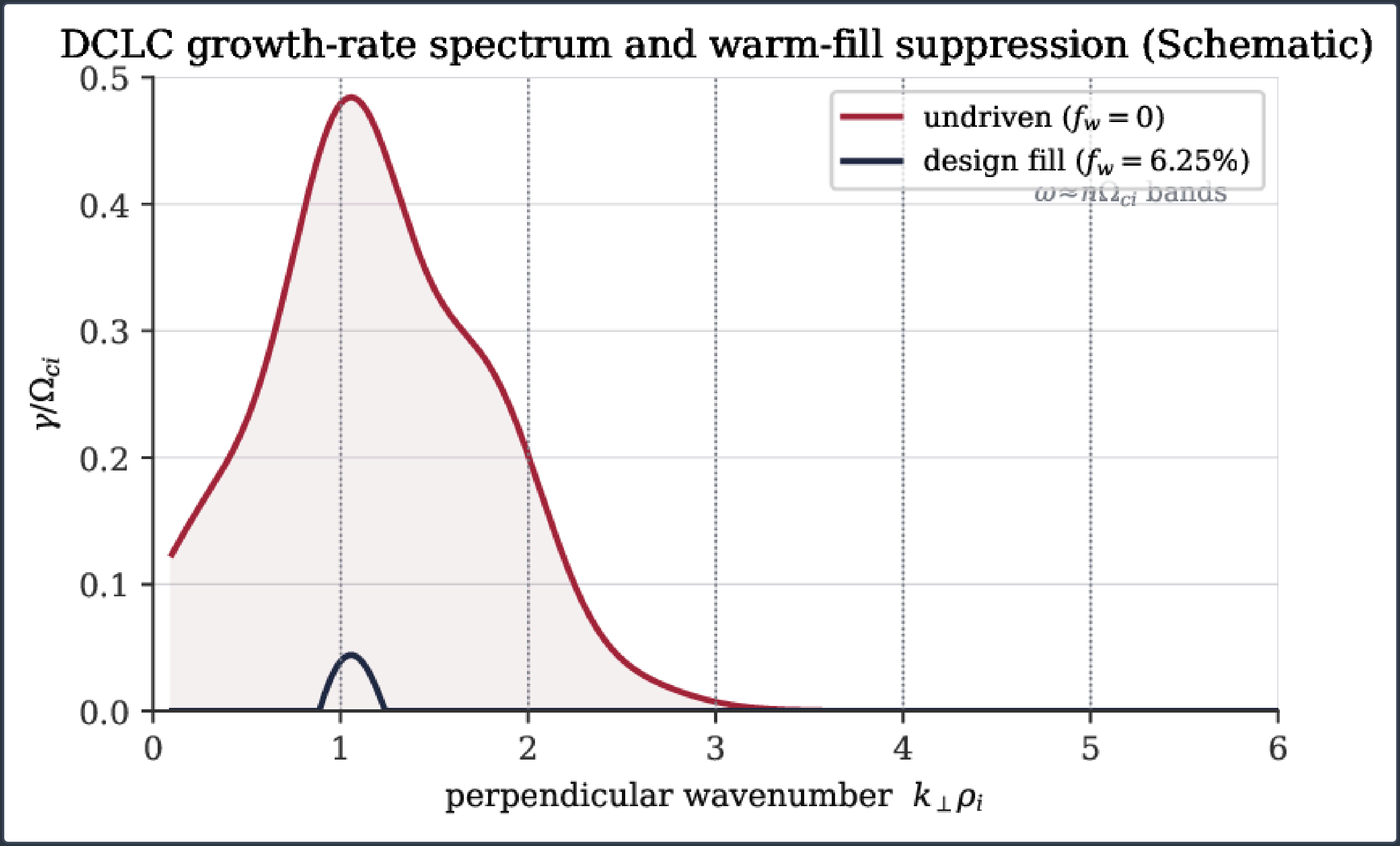

DCLC growth-rate spectrum and warm-fill suppression (Schematic). The undriven spectrum (red) is unstable in a band near $k_\perp\rho_i \sim 1$ with structure at the cyclotron harmonics $\omega \approx n\Omega_{ci}$; the design warm fill (navy) pushes the spectrum below marginal.

§ 6

Discussion

AGAINST THE MIRROR RECORD

The result reproduces, quantitatively, the lesson of the mirror program: warm-plasma streaming stabilizes DCLC. 2XIIB found that a warm-plasma fraction of a few percent quenched a violently unstable plug [3,4]; the Kronos plug requires $f_{\text{crit}} = 5.96–6.78\%$ across the demanding gradient range (Table 2), squarely in that historical band. The mechanism, the gradient-scale dependence, and the sharpness of the boundary all match the classical picture of Post–Rosenbluth and Baldwin [1,2]. Where the present work goes beyond the historical estimate is in mapping the exact boundary with a modern kinetic solver and anchoring it with first-principles PIC, so that the design's distance from the boundary is a measured number ($L_n/\rho_i = 25.3$) rather than an order-of-magnitude expectation.

THE AIC RESIDUAL IN CONTEXT

That a warm fill quenches DCLC but not the anisotropy-driven ion-cyclotron branch is exactly what the theory of Eqs. (10)–(11) predicts, and it echoes the 2XIIB observation of residual ion-cyclotron fluctuations in the warm-plasma-stabilized regime [12,13]. The measured residual $\gamma/\Omega_{ci} \approx 0.037$ at $\beta_\perp \approx 0.5$, $A = 2$ is a weak, marginal-anisotropy mode, and its insensitivity to f_w (Fig. 5) is the signature that distinguishes it from DCLC. Its factor ~ 13 separation from the DCLC amplitude, and its monotonic suppression by an energetic stabilizer (Fig. 6), place it in the category of a managed residual rather than a binding limit.

RELATION TO THE BURNER DESIGN AND ITS CONTROLLERS

The plug microstability gate is separable from the burner's neutron-source performance: the neutron fraction $f_n = 5.44\%$ and the engineering gain $Q_E = 1.318$ do not depend on where the plug sits relative to its DCLC boundary [28]. What the gate binds is the plug-*potential* route to axial confinement, since a DCLC-unstable plug cannot hold its potential. The design response is twofold: hold the warm fill near 6.25% (a fueling/actuator task addressed by the RF alpha-channeling and plug-potential work [30,31,32]), and hold the operating point inside the boundary with the real-time DCLC/AIC microstability controller [34], whose acceptance test is precisely that the operating point stays inside the boundary mapped here. The energetic-stabilizer end-cell of Eq. (17) is the physics basis for the AIC actuator [33]. This paper supplies the boundary those controllers must respect.

§ 7

Limitations

The dispersion analysis is linear and local: it identifies marginal stability, not the nonlinear saturated state, and does not resolve finite-$k_\parallel$ or geometric-mirror effects beyond the flute limit. The full six-dimensional velocity-space eigenmode is captured by the PIC cross-check but not by the reduced dispersion scan. The gradient scale L_n/ρ_i is treated as a free parameter because it is set by plug-edge profiles that a transport calculation — not this stability calculation — must supply; the honest single open gate is that the plug-edge gradient at which the plug actually operates is an input to, not an output of, this analysis, and the design's marginal pass is conditional on $L_n/\rho_i \gtrsim \mathbf{25.3}$. The warm-fill fraction is likewise a model input; delivering and sustaining $\mathbf{6.25\%}$ is an actuator question left to the plug engineering. Finally, the plug-*potential* requirement itself — the separate binding gate that the plug can raise a sufficient ϕ_p — is not addressed here and is not claimed retired.

§ 8

Conclusion

Warm-plasma streaming stabilizes the DCLC loss-cone mode of the Kronos D–^{3}He tandem-mirror burner plug through a sharp, monotonic boundary, and the burner's $\mathbf{6.25\%}$ warm fill sits exactly on that knee, clearing DCLC only for plug-edge gradients $L_n/\rho_i \gtrsim \mathbf{25.3}$ and leaving an on-knee residual of $\approx \mathbf{0.034}\,\Omega_{ci}$ at the demanding gradient. A weak, anisotropy-driven AIC residual at $\gamma/\Omega_{ci} \approx \mathbf{0.037}$ persists flat across the warm fill in both the electrostatic dispersion solver and two independent PIC codes, roughly an order of magnitude below the DCLC rate, and is quenched monotonically by an energetic kinetic stabilizer. The plug microstability is therefore marginal but bounded, and quantified against a definitive stability boundary — a single measured number, $(L_n/\rho_i)_c = \mathbf{25.3}$ — rather than asserted. The stabilizing lever, the sensitive parameter, and the residual electromagnetic branch are all identified, and the design's distance from its microstability boundary is now a controllable quantity.

Acknowledgments tocsectionAcknowledgments Part of the Kronos Fusion Energy 2026 design series. The authors thank the Kronos physics de-risking programme for the frozen result set underlying every quantitative claim, and acknowledge the developers of the open LEOPARD, WarpX, and Smilei codes on which the computational methodology is built.

Reproducibility. Every headline quantity in this paper is a frozen anchor (BU-L2-A5, BU-L2-A7, AG-CX-03/07) in the Kronos Physics De-Risking Register [27] (doi:10.5281/zenodo.22133057) and is regenerable from the archived dispersion solvers, PIC loading scripts, and marginal-boundary scan deposited with this paper. This paper is archived at its DOI doi:10.5281/zenodo.22645714; official version: https://www.kronosfusionenergy.com/publications/dclc-loss-cone-microstability.html and its official page https://www.kronosfusionenergy.com/publications/dclc-loss-cone-microstability.html. No result depends on unpublished or proprietary data, and no economic analysis is included in the public deposit.

Scope — what this paper does not claim. The plug microstability is stated as marginal (on the stabilization knee) with a residual AIC mode carried, not as comfortably stable; the plug-potential requirement is a separate gate and is not addressed here.

Data availability tocsectionData availability The marginal-boundary scan, the residual-growth data, the AIC and kinetic-stabilizer sweeps, and the figure-generation script used for Figs. 1–9 are archived with the deposit for this paper at doi:10.5281/zenodo.22645714, whose official page is https://www.kronosfusionenergy.com/publications/dclc-loss-cone-microstability.html. All quantitative values trace to the de-risking register [27] by the serial identifiers cited inline.

Competing interests tocsectionCompeting interests Provisional patent applications relating to aspects of this work have been filed.

tocsectionReferences

APPARATUS

Portfolio, People & Record

The intellectual-property estate, the people who built it, the limitations that gate it, and the sources it rests on.

1	4	40	27
GRANTED PATENT	2026 PROVISIONALS	TEAM MEMBERS	2022 PROVISIONALS

INTELLECTUAL PROPERTY

The patent portfolio

The estate spans a granted high-field magnet patent, pending utility and 2026 provisional filings that map to the two products, a digital-twin control provisional, a registered trademark application, and the original 2022 provisional family. Every patentable disclosure in the five-paper arXiv drop was protected **before** publication: the breeder and burner provisionals were filed 1–2 August, and a publication-gap omnibus filing the evening before the drop swept up the DEC, plasma-control, and REBCO-winding matter of the three otherwise-unprotected papers. Patent numbers and application serials are matters of public record; claim scope is summarised, not reproduced.

GRANTED & PENDING UTILITY

US 12,009,112	High-field tilted graded-REBCO magnet architecture (KRONO-002A) · *app. 17/878,550*	GRANTED
US 17/878,507	Core device / method (KRONO-001A) · *utility*	PENDING

2026 PROVISIONAL FILINGS — MAPPED TO THE PRODUCTS

64/124,209	Hyperion — spherical-tokamak tritium / helium-3 foundry · *breeder · filed Aug 2026*	FILED
64/124,220	Aegis / MetroVolt — synchrotron-cutoff, fuel-selection & plug-winding · *generator · filed Aug 2026*	FILED
64/115,167	KRONOS-CTRL digital-twin plant control · *provisional · filed Jul 2026*	FILED
64/005,440	Integrated spherical-tokamak fusion architecture · *early integrated-architecture filing · filed Mar 2026*	FILED
64/105,530	Negative-triangularity spherical-tokamak architecture · *foundational ST filing · filed Jul 2026*	FILED
64/128,097	Publication-gap omnibus — quasineutral two-species expander DEC · provenance-gated / latency-split plasma control · as-built high-field winding & conductor architecture · *filed 7 Aug 2026, the evening before the arXiv drop*	FILED

TRADEMARK & ORIGIN

FTK-98801894	Kronos Fusion Energy — trademark application	FILED
KR-2022-*	Original provisional family (KR-2022-00001 … 00027) · *27 filings, 2022*	PRIORITY

The narrow, defensible magnet novelty — the specific conductor and the digital-twin winding optimisation, not high-field REBCO as a category — is the commercial core that can earn ahead of any Q > 1 milestone, with markets in fusion magnet supply, MRI/NMR, accelerators, and proton therapy. The claim is scoped honestly: the high field is a *system field* result, not a stand-alone-coil record; the small-bore plug coil is structurally infeasible as a bare winding but resolved by a stress-managed structural shield (feasible-pending-FEA); and the winding-tape experiment returned a *null result*. The value is the method, not a field record.

THE TEAM

Founding partners, board, advisors & auditors

Kronos is built by a bench of advanced-fuel-fusion, high-field-magnet, direct-conversion, and materials specialists, with a board and operations team drawn from defense, national laboratories, and industry. Dates are shown as ranges; where a tenure has ended or is term-ending, the range says so.

FOUNDING PARTNERS — SCIENCE

Dr. Gerald Kulcinski
Co-Founder · Helium-3 & Advanced-Fuel Fusion
UW–Madison · 2023–Present

Dr. Carl Weggel
Chief Scientist / S.M.A.R.T. Design
MIT Alcator Program · 2022–Present

Dr. Robert J. Weggel
Magnetic Field Design
MIT Magnet Lab · 2022–Present

BOARD

Priyanca Ford
Founder & CEO · Executive Board
2022–Present

Bandel Carano
Finance / Strategy
Oak Investment Partners / Stanford · 2025–2026

Patrick Schweiger
Fusion Device Engineering
Oklo / CFS / TerraPower · 2025–Present

SCIENTIFIC ADVISORS

Dr. Steven O. Dean
Fusion Policy & History
DOE / Fusion Power Associates · 2025–Present

Dr. Patrick H. Diamond
Plasma Turbulence & Transport
UC San Diego · 2025–Present

Dr. Jack J. Dongarra
HPC & Numerical Algorithms
Turing Award · 2025–Present

Dr. Nasr M. Ghoniem
Chief Material Scientist
UCLA · 2025–Present

Dr. Siegfried Glenzer
Plasma Physics & Laser Fusion
Stanford / SLAC · 2022–Present

Dr. David A. Hammer
Pulsed-Power Fusion
Cornell · 2025–Present

Dr. Donald A. Spong
Plasma Theory & Confinement
ORNL · 2025–Present

Dr. Curtis Smith
Risk Assessment & Nuclear PRA
MIT / Idaho National Lab · 2025–Present

RADM (Ret.) David Goggins
Naval Engineering & Power-Plant Design
U.S. Navy · 2023–2026

Dr. Konstantin Batygin
Mathematician
Caltech · 2022–2025

Dr. Ruben Fair
Magnet Design / ITER Liaison
PPPL / Jefferson Lab · 2022–2025

Dr. Paul S. Weiss
Materials & Nanotechnology
UCLA · 2022–2025

SCIENTIFIC AUDITORS

Dr. Wilfred A. Cooper
Plasma Equilibrium Theory
EPFL / Swiss Plasma Center · 2025–Present

Dr. Ahmed Hassanein
Plasma–Material Interactions
Purdue / Argonne · 2025–Present

Dr. Patrick E. Hopkins
Extreme Thermal Materials
U. of Virginia · 2025–Present

Dr. Peter Hosemann
Materials Joining & Structural Integrity
UC Berkeley · 2025–Present

Dr. Travis W. Knight
Advanced Nuclear Fuels & Systems
U. of South Carolina · 2025–Present

Dr. Philippe Lebrun
Cryogenics & Magnet Cooling
CERN · 2025–Present

Dr. Nitendra Singh
Nuclear Safety & Fuel Cycle
ITER · 2025–Present

Dr. Guido Van Oost
Magnetic Confinement & Fusion Systems
Ghent University · 2025–Present

Dr. Gary S. Was
Radiation Materials & Structural Integrity
U. of Michigan · 2025–Present

Dr. Ray Sedwick
Direct Energy Conversion
U. of Maryland · 2025

OPERATIONS

Michael Laughlin
Chief Operating Officer
2022–Present

Martin Owens
Chief Strategy Officer
LANL / GE Hitachi · 2022–Present

MG (Ret.) Paul Pardew
Chief Contracting Officer
Army Contracting Command · 2022–Present

David Beck
Fusion Commercialization
U.S. Space Force · 2024–Present

Sushma Bhatia
Environmental & Legislative
Google · 2022–Present

Michael De Frenza
Technology Licensing
2023–Present

MG (Ret.) Robin L. Fontes
Cybersecurity & Defense
Army Cyber Command · 2022–Present

Vijay Gehani
Supply Chain & Components
INOX India · 2024–Present

Jon Michel Greenwood
IT & AI Infrastructure
Live Nation · 2023–Present

Brian C. O'Neill
National Security
CIA / ODNI · 2022–Present

Gen. (Ret.) Gustave F. Perna
DoD Liaison
Operation Warp Speed · 2022–2023

Andrea Romero
Marketing Lead
2022–Present

Legal counsel is retained; those roles are held on the internal roster and are not listed here.

SOURCES

References

1 R F Post and M N Rosenbluth, Electrostatic instabilities in finite mirror-confined plasmas, *Phys. Fluids* **9** 730 (1966). doi:10.1063/1.1761740

2 D E Baldwin, End-loss processes from mirror machines, *Rev. Mod. Phys.* **49** 317 (1977). doi:10.1103/RevModPhys.49.317

3 F H Coensgen, W F Cummins, B G Logan *et al*, Stabilization of a neutral-beam-sustained, mirror-confined plasma, *Phys. Rev. Lett.* **35** 1501 (1975). doi:10.1103/PhysRevLett.35.1501

4 D E Baldwin, H L Berk and L D Pearlstein, Turbulent lifetimes in mirror machines, *Phys. Rev. Lett.* **36** 1051 (1976). doi:10.1103/PhysRevLett.36.1051

5 D E Baldwin and B G Logan, Improved tandem mirror fusion reactor, *Phys. Rev. Lett.* **43** 1318 (1979). doi:10.1103/PhysRevLett.43.1318

6 M Inutake *et al*, Thermal barrier formation and plasma confinement in the axisymmetrized tandem mirror GAMMA-10, *Phys. Rev. Lett.* **55** 939 (1985). doi:10.1103/PhysRevLett.55.939

7 R F Post, The magnetic mirror approach to fusion, *Nucl. Fusion* **27** 1579 (1987). doi:10.1088/0029-5515/27/10/001

8 P Astfalk and F Jenko, LEOPARD: a grid-based dispersion relation solver for arbitrary gyrotropic distributions, *J. Geophys. Res. Space Physics* **122** 89 (2017). doi:10.1002/2016JA023522

9 J-L Vay *et al*, Warp-X: a new exascale computing platform for beam–plasma simulations, *Nucl. Instrum. Methods Phys. Res. A* **909** 476 (2018). doi:10.1016/j.nima.2018.01.035

10 J Derouillat *et al*, SMILEI: a collaborative, open-source, multi-purpose particle-in-cell code for plasma simulation, *Comput. Phys. Commun.* **222** 351 (2018). doi:10.1016/j.cpc.2017.09.024

11 R C Davidson and J M Ogden, Electromagnetic ion cyclotron instability driven by ion energy anisotropy in high-beta plasmas, *Phys. Fluids* **18** 1045 (1975).

12 T A Casper and G R Smith, Observation and analysis of the Alfv\'en ion-cyclotron instability in the 2XIIB mirror experiment, *Phys. Rev. Lett.* **48** 1015 (1982).

13 S P Gary and M A Lee, The ion-cyclotron anisotropy instability and the marginal stability constraint, *J. Geophys. Res.* **99** 11297 (1994).

14 S P Gary, *Theory of Space Plasma Microinstabilities* (Cambridge: Cambridge University Press, 1993).

15 T H Stix, *Waves in Plasmas* (New York: American Institute of Physics, 1992).

16 B D Fried and S D Conte, *The Plasma Dispersion Function* (New York: Academic Press, 1961).

17 C K Birdsall and A B Langdon, *Plasma Physics via Computer Simulation* (New York: McGraw-Hill, 1985).

18 G I Dimov, V V Zakaidakov and M E Kishinevsky, Thermal insulation of plasma in a mirror trap, *Sov. J. Plasma Phys.* **2** 326 (1976).

19 T K Fowler and B G Logan, The tandem mirror reactor, *Comments Plasma Phys. Control. Fusion* **2** 167 (1977).

20 T K Fowler, R W Moir and T C Simonen, A new simpler way to obtain high fusion power gain in tandem mirrors, *Nucl. Fusion* **57** 056014 (2017).

21 D Endrizzi *et al*, Physics basis for the Wisconsin HTS Axisymmetric Mirror (WHAM), *J. Plasma Phys.* **89** 975890501 (2023).

22 J E Menard *et al*, Fusion nuclear science facilities and pilot plants based on the spherical tokamak, *Nucl. Fusion* **56** 106023 (2016). doi:10.1088/0029-5515/56/10/106023

23 B N Sorbom *et al*, ARC: a compact, high-field, fusion nuclear science facility and demonstration power plant with demountable magnets, *Fusion Eng. Des.* **100** 378 (2015). doi:10.1016/j.fusengdes.2015.07.008

24 A J Creely *et al*, Overview of the SPARC tokamak, *J. Plasma Phys.* **86** 865860502 (2020). doi:10.1017/S0022377820001257

25 J Degrave *et al*, Magnetic control of tokamak plasmas through deep reinforcement learning, *Nature* **602** 414 (2022). doi:10.1038/s41586-021-04301-9

COLOPHON

How this document was made

The Kronos Fleet — Combined Editorial, 2026 is set in **Fraunces** (display), **Gelasio** (text), and **IBM Plex Mono** (data & equations), carried forward from the Kronos editorial design system.

The figures are rendered at 300 dpi from the deposited generator scripts; the document is composed as a single self-contained file with embedded fonts and imagery, paginated to US Letter, and rendered to PDF through a headless Chromium engine in matched light and dark editions.

Every headline quantity carries an evidence class; withdrawn and restated values are marked as such. Nothing herein is frozen beyond the founder-approved Tier-A set.

Explore it live — turn the interactive 3-D model, run the deposited solvers in the physics validator, and watch the companion film series.

LEGAL NOTICE

Notice, status, and distribution

Conceptual design & simulation study. This document reports a conceptual design and simulation study. It is not a construction commitment, a safety-analysis report, a regulatory filing, or an offer of securities. Forward-looking statements — schedules, costs, market sizes, and performance — are estimates subject to the limitations set out in the Simulations part and may change.

Numbers and their classes. Quantities are reported with evidence classes and case labels; modelled, assumed, and requirement-class values are identified as such and are not to be quoted without their labels.

Public edition. This edition carries the physics and design only; all financial, funding, and defense-commercial content has been removed for public distribution. The scientific text corresponds to the arXiv and journal submissions.

THE 2026 KRONOS SERIES

One programme, many papers

This editorial is one paper in the Kronos 2026 series — a real fusion company's complete, reproducible physics record for a spherical-tokamak breeder and its low-neutron D–^{3}He tandem-mirror burners. Every headline number is a frozen anchor in the Physics De-Risking Register.

Explore the whole programme: the De-Risking Register, the interactive 3-D model, and the physics validator.

KRONOS FUSION ENERGY

Velocity-Space Microstability at the DCLC Knee: Warm-Fill Requirements and Residual AIC Activity in a D–^{3}He Tandem-Mirror Burner

A real fusion company building real machines. Explore the science, live.

Zenodo · doi:10.5281/zenodo.22645714

Read on kronosfusionenergy.com

The Physics De-Risking Register